Chapter

High-Entropy Ceramics

Sajid Ali Alvi, Hanzhu Zhang and Farid Akhtar

Abstract

High-entropy ceramics is an emerging class of high-entropy materials with properties superior to conventional ceramics. Recent research has been focused on the development of new high-entropy ceramic compositions. High-entropy oxides, carbides, borides, silicides, and boron carbides had been reported with superior mechanical, oxidation, corrosion, and wear properties. The research work on the processing and characterization of bulk high-entropy ceramics and coating systems has been summarized in this chapter. The composition design, structure, chemistry, composite processing of bulk high-entropy ceramics, and evolution of microstructure and properties are reported. The literature on the deposition of high-entropy ceramic coating and the influence of coating parameters have been discussed to produce high-entropy ceramic coatings with superior mechanical, oxidation, and wear properties.

Keywords: ceramics, spark plasma sintering, coatings, high temperature properties

1. Introduction

The concept of high-entropy alloy (HEA), an alloy with five or more constituents with a concentration between 5 and 35%, has triggered extensive research to develop new metallic and ceramic high-entropy materials. Like HEAs, high-entropy ceramics (HECs) consist of multicomponent ceramic oxides, borides, and nitrides. The HECs exhibit homogeneous crystalline single-phase despite the complex structure of ceramic compounds and offer superior properties over the constituents and conventional ceramics. The development of high-entropy ceramic coatings is an important route to design new and novel high-entropy ceramic materials with superior properties for practical applications. In this chapter, the recent work on HECs is summarized in the following two sections: bulk HECs and HEC coatings. Bulk HEC section is focused on the processing and the evolution of significantly enhanced mechanical properties of borides, oxides, and carbide ceramics and composites. Moreover, the potential of HECs in thermal-electrical, tribological, and high temperature applications are discussed. In the section on high-entropy coatings, recently reported researches on different HEC coating techniques and the properties of the HEC coatings have been summarized.

2. Bulk high-entropy ceramics

2.1 Fabrication routes

The fabrication of HEAs can be achieved through solid and liquid state routes. The processing of bulk HECs is preferred in solid state due to the high melting

points of ceramics. The solid-state processing includes high energy ball milling, conventional solid state sintering, self-propagating high temperature synthesis (SHS), and spark plasma sintering (SPS) under the combined effect of heating using electric current and pressure. The SPS is a rapid and facile method to produce nearly dense components and suitable for sintering of high-entropy ceramics. Typically, the precursor ceramic powders are mixed and filled into a graphite die and rapidly sintered under high vacuum, pulsed direct electrical current, and uniaxial pressure.

Different types of the ceramic precursors have been used to fabricate HECs. The most commonly used precursors are commercial ceramic powders. The ceramic powders are mixed in desired stoichiometric ratio and homogenized using ball milling followed by spark plasma sintering to a target temperature and uniaxial pressure. The synthesis of high-entropy ceramic powders has been investigated as well. The precursor ceramic powders can be pre-synthesized via thermal reduction (TR) where metal oxide powders are used as reactants (**Figure 1**). The advantages of using oxide powders as raw materials include reducing the cost of the starting materials and possibilities of producing high purity ceramic powders with controlled grain size. Feng et al. [1] used metallic oxides and carbon black powder as starting material to produce high-entropy (Hf, Zr, Ti, Ta, Nb)C powder. The carbothermal reduction of oxide ceramics was completed at 1873 K under vacuum in 1 hour. Subsequent solid solution formation was achieved at a higher temperature of 2273 K, demonstrating a single-phase rocksalt structure of the solid solution. Ye et al. [2] reported the synthesis of high-entropy $(Zr_{0.25}Ta_{0.25}Nb_{0.25}Ti_{0.25})C$ powders of a single-phase rocksalt crystal structure by carbothermal reduction of metal oxides and graphite.

Liu et al. [3] demonstrated the synthesis of high-entropy $(Hf_{0.2}Zr_{0.2}Ta_{0.2}Nb_{0.2}Ti_{0.2})B_2$ powders with single-phase hexagonal structure through borothermal reduction from metal oxides and amorphous boron powders at 1973 K under argon atmosphere. The synthesized high-entropy metal diboride powders showed a fine particle size of 310 nm. Instead of boron, Zhang et al. [4] used the combination of B_4C, graphite, and metal oxides to synthesize $(Hf_{0.2}Zr_{0.2}Ta_{0.2}Nb_{0.2}Ti_{0.2})B_2$, $(Hf_{0.2}Zr_{0.2}Mo_{0.2}Nb_{0.2}Ti_{0.2})B_2$, and $(Hf_{0.2}Mo_{0.2}Ta_{0.2}Nb_{0.2}Ti_{0.2})B_2$ powders by boro-/carbothermal reduction. The reaction is reported to be more effective than borothermal reduction, with a lower reduction temperature 1873 K.

Wei et al. synthesized high-entropy carbide $(Ti_{0.2}Zr_{0.2}Nb_{0.2}Ta_{0.2}W_{0.2})C$ by employing different methods using commercial carbide powders and thermally reduced carbide powders and *in-situ* fabrication process from elemental powders [5]. All three compositions revealed single-phase face-centered cubic (FCC) structure according to X-ray diffraction (XRD) patterns. The comparison of the

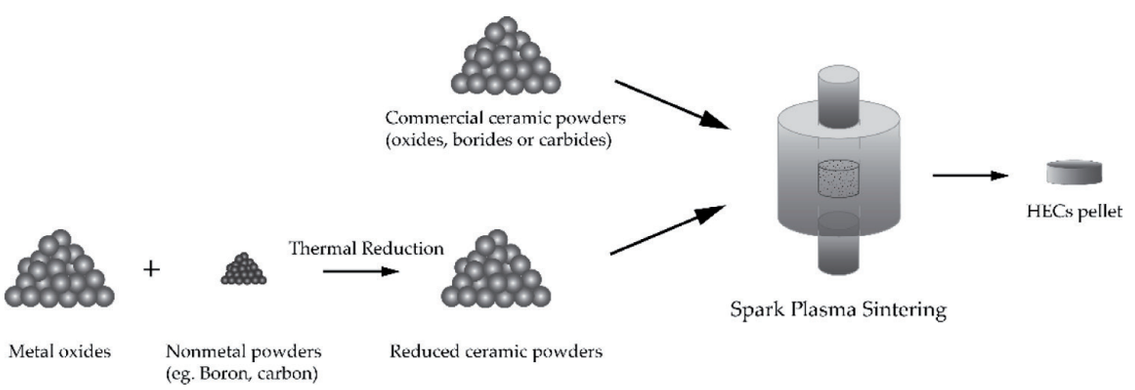

Figure 1.
The fabrication routes of dense high-entropy ceramics.

three methods suggested the microstructure inhomogeneity in case of elemental powders and TR approach.

2.2 Overview of current researches on bulk HECs

2.2.1 High-entropy oxides (HEOs)

The first high-entropy ceramic was reported by Rost et al. [6], on the production of entropy stabilized metal oxides with rocksalt crystal structure, synthesized from equimolar CoO, CuO, MgO, NiO, and ZnO in a tube furnace at temperatures above 850°C. Homogenous distribution of the cations in the crystal structure was observed. The system showed a reversible transformation between the high-entropy solid solution and multicomponent oxide mixture. Later on, detailed investigation using extended X-ray absorption fine structure (EXAFS) was performed to investigate the localize structure of the aforementioned high-entropy oxide [7], demonstrating that the anion lattice (O sublattice) has the most distortion to accommodate the size mismatch in the cation lattice (metal sublattice). The phase stability, as a result of configurational entropy, of the same HEO system was studied by Anand et al. [8].

The entropy stabilized oxide ((Mg, Ni, Co, Cu, Zn)O with colossal dielectric constant was discovered by Bérardan et al. [9]. With a Li^+ ionic conductivity of $>10^{-3}$ S/cm, which is much higher compared to lithium phosphorous oxynitride (LiPON) solid electrolyte (2×10^{-6} S/cm) [10], the produced high-entropy oxide was suggested to be an excellent substituent as superionic conductors for Li^+ and Na^+. The potential of high-entropy oxide in the lithium battery has been reported by Sarkar et al. [11] with improved storage capacity retention and cycling stability.

Jiang et al. [12] synthesized high-entropy perovskite oxides from multiple ABO_3 perovskite oxides. Djenadic et al. [13] utilized nebulized spray pyrolysis (NSP) to synthesize single-phase rare earth oxide powders from seven equiatomic rare earth oxides. In the REO system, the importance of selecting the starting component in the reported multicomponent oxide system was highlighted, with cerium (Ce^{4+}) addition being confirmed to improve the formation of single-phase solid solution. Gild et al. [14] fabricated high-entropy fluorite oxides from five fluorite oxides via high-energy ball milling and SPS, followed by various annealing treatments. Most of the fabricated HEOs revealed as nearly fully dense pellets with single-phase Fm-3 m crystal structure. Phonon scattering effect in the HEO system resulted in low thermal conductivity, making the synthesized HEOs desirable for thermal insulation applications.

2.2.2 High-entropy borides (HEBs)

The high-entropy borides are designed and fabricated from transition metal diborides, HfB_2, ZrB_2, TaB_2, etc., aiming at developing a new class of ultrahigh temperature metal diboride materials with superior mechanical properties over conventional diborides.

Gild et al. [15] sintered HEBs from five-component equimolar metal diborides via SPS. The fabricated HEBs from compositions like $(Hf_{0.2}Zr_{0.2}Ta_{0.2}Mo_{0.2}Ti_{0.2})B_2$ and $(Mo_{0.2}Zr_{0.2}Ta_{0.2}Nb_{0.2}Ti_{0.2})B_2$ possess single-phase hexagonal AlB_2 structure (**Figure 2**) as the parent metal diborides, with alternating hexagonal metal cations net and rigid boron net in the high-entropy structure. The authors reported that in case of using W_2B_5 in the starting precursors, single-phase solid solution was not successfully formed. Notably, W_2B_5 has a different crystal structure with other utilized metal borides, as well as limited solubility in other borides, which could

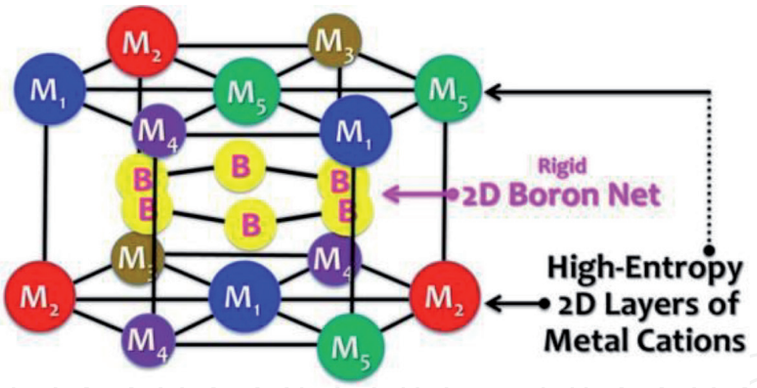

Figure 2.
The hexagonal AlB_2 structure of HEBs by Gild et al. [15] (licensed under CC BY 4.0, https://doi.org/10.1038/srep37946).

be potential factors of the formability of single-phase solid solution in the HEB system. The fabricated HEBs show improved hardness and oxidation resistance as compared to the average performances of the constituent borides.

The crystal structure, mechanical, and electronic properties of the HEB $(Hf_{0.2}Zr_{0.2}Ta_{0.2}M_{0.2}Ti_{0.2})B_2$ (M = Nb, Mo, Cr) were investigated by Sarkar et al. using ab initio calculations [16]. In the unique layered hexagonal lattice structure shown in **Figure 2**, the metal layer and 2D boron layer contain metallic bonds and covalent bonds, respectively, while both ionic and covalent bond were found between the two hexagonal layers. The high stability of the studied HEBs is contributed by strong boron-boron bond and metal-boron bond. Density-functional theory (DFT) calculations suggested negligible solid solution strengthening effect in elastic modulus, showing similar value with elastic modulus calculated by the mixing rule.

Tallarita et al. [17] synthesized bulk HEB $(Hf_{0.2}Mo_{0.2}Ta_{0.2}Nb_{0.2}Ti_{0.2})B_2$ by self-propagating high-temperature synthesis (SHS) from elemental metal and boron powders, followed by SPS at 2223 K. High fraction of high-entropy phase with hexagonal (space group P6/mmm) was obtained after the SHS process, along with minor amount of binary diborides and metal oxides. The SHS powders showed good sinterability with a relative density of 92.5% in the SPS product. The sintered HEB exhibits a single-phase hexagonal crystal structure which is similar to the hexagonal AlB_2 structure reported by Gild et al. [15], with improved hardness (22.5 ± 1.7 GPa) and oxidation resistance. The authors mentioned that the single-phase structure could not be obtained when performing one-step reactive SPS process with the same reactants.

Based on the developed HEB system, Zhang et al. [18] adopted borothermal reduction process to synthesize high-entropy borides from metal oxides and amorphous boron powder, aiming at producing ultra-fine HEB powder with improved sinterability. The obtained HEB powders $(Hf_{0.2}Zr_{0.2}Ta_{0.2}Cr_{0.2}Ti_{0.2})B_2$, $(Hf_{0.2}Mo_{0.2}Zr_{0.2}Nb_{0.2}Ti_{0.2})B_2$, and $(Hf_{0.2}Mo_{0.2}Ta_{0.2}Nb_{0.2}Ti_{0.2})B_2$ showed an average particle size smaller than 1 μm and led to final relative densities greater than 95% in the SPS products. The sintered HEBs showed ultrahigh hardness values of 28.3, 26.3, and 25.9 GPa, respectively. Compared to the HEBs with same compositions sintered from −325 mesh diboride powders by Gild et al. [15] (about 22 GPa), these HEBs have improved hardness properties as a result of utilization of ultrafine starting particles in SPS.

2.2.3 High-entropy carbides

The first reported high-entropy carbides were synthesized from transition metal carbides HfC, TaC, ZrC, NbC, and TiC by Castle et al. [19]. Four-component metal

carbides were mixed in equiatomic ratio using high-energy ball milling and sintered in SPS with a maximum sintering temperature of 2573 K to form high-entropy (Hf-Ta-Zr-Ti)C and (Hf-Ta-Zr-Nb)C ultra-high temperature carbides. A single-phase solid solution with a rocksalt crystal structure was formed. More complete inter-diffusion in the formation of single-phase solid solution was found in the (Hf-Ta-Zr-Nb)C than (Hf-Ta-Zr-Ti)C system. As the atomic radius of Ti, as well as the lattice parameter of TiC is the smallest among the five starting components, the effect of lattice mismatch among the starting metal carbides on formability of high-entropy solid solution was highlighted. By considering the metal atomic radii, melting points and vacancy formation energy of the carbides, it is believed that TaC, which has the lowest metal vacancy formation energy, acted as the host lattice during the diffusion, while other metal atoms migrate into TaC lattice and occupy the cation positions. The nanoindentation of the fabricated high-entropy (Hf-Ta-Zr-Nb)C shows a hardness of 36.1 ± 1.6 GPa, which is 30% higher than the theoretical value calculated from the rule of mixture. Low thermal conductivity was observed in the reported SPS high-entropy carbides. Further investigation on the microstructure, atomic structure, and localized chemical disorder of the fabricated four-component high-entropy (Hf-Ta-Zr-Nb)C was reported by Dusza et al. [20]. Homogeneity of the chemical composition in both micro- and nanoscale was proved by various experimental approaches including scanning electron microscopy (SEM), transmission electron microscopy (TEM), and electron backscattered diffraction (EBSD).

The low thermal conductivity and diffusivity behavior were observed by Yan et al. [21] in the five-component high-entropy $(Hf_{0.2}Zr_{0.2}Ta_{0.2}Nb_{0.2}Ti_{0.2})C$ ceramic. The high-entropy carbide was synthesized in SPS at 2273 K and displayed rocksalt crystal structure with the metal atoms occupying the cation positions, while carbon occupied the anion positions in the lattice. The measured thermal diffusivity is reported to be lower than monocarbides and even some of the binary carbides. The increased number of principal elements in the structure led to lattice distortion, mainly through the carbon sublattice, which consequently caused severe phonon scattering. The same high-entropy carbide $(Hf_{0.2}Zr_{0.2}Ta_{0.2}Nb_{0.2}Ti_{0.2})C$ in powder form was synthesized by Zhou et al. [22] via pressureless sintering in SPS.

Entropy-forming-ability (EFA), the first systematic criterion to determine relative propensity of a multicomponent (metal carbide) system to form a high-entropy single-phase crystal structure was introduced by Sarker et al. [23], published on Nature Communication in November 2018. A total of 56 five-component systems from 12 metal carbides (Hf, Nb, Mo, Ta, Ti, V, W, and Zr) were investigated in the work by evaluating the energy distribution spectra of the structures that were generated by the AFLOW-POCC (automatic FLOW partial occupation) [24] algorithm. A narrow spectrum suggests low energy barrier to introduce more configurational disorder, thereby displays high EFA value. The calculation results were verified by synthesizing nine from the 56 compositions in SPS at 2473 K and comparing the experimental and calculation results. The phase identification in **Figure 3** suggested that six compositions $MoNbTaVWC_5$, $HfNbTaTiZrC_5$, $HfNbTaTiVC_5$, $NbTaTiVWC_5$, $HfNbTaTiWC_5$, and $HfTaTiWZrC_5$ that have higher EFA values than the rest three compositions reveals single-phase rocksalt crystal structure after SPS, while secondary phases were observed in compositions $HfMoTaWZrC_5$, $HfMoTiWZrC_5$, and $HfMoVWZrC_5$ with low EFA values.

The *ab initio* entropy descriptor invented by Sarker et al. [23] provides a new understanding of the formation of single-phase high-entropy materials and offers a systematic guide for researchers to design high-entropy carbides. Group IV and V carbides are known to have nearly complete mutual solubility; therefore, the formation of single-phase solid solution is relatively probable, attributed to enthalpy stabilization. Meanwhile, the incorporation of carbides with different

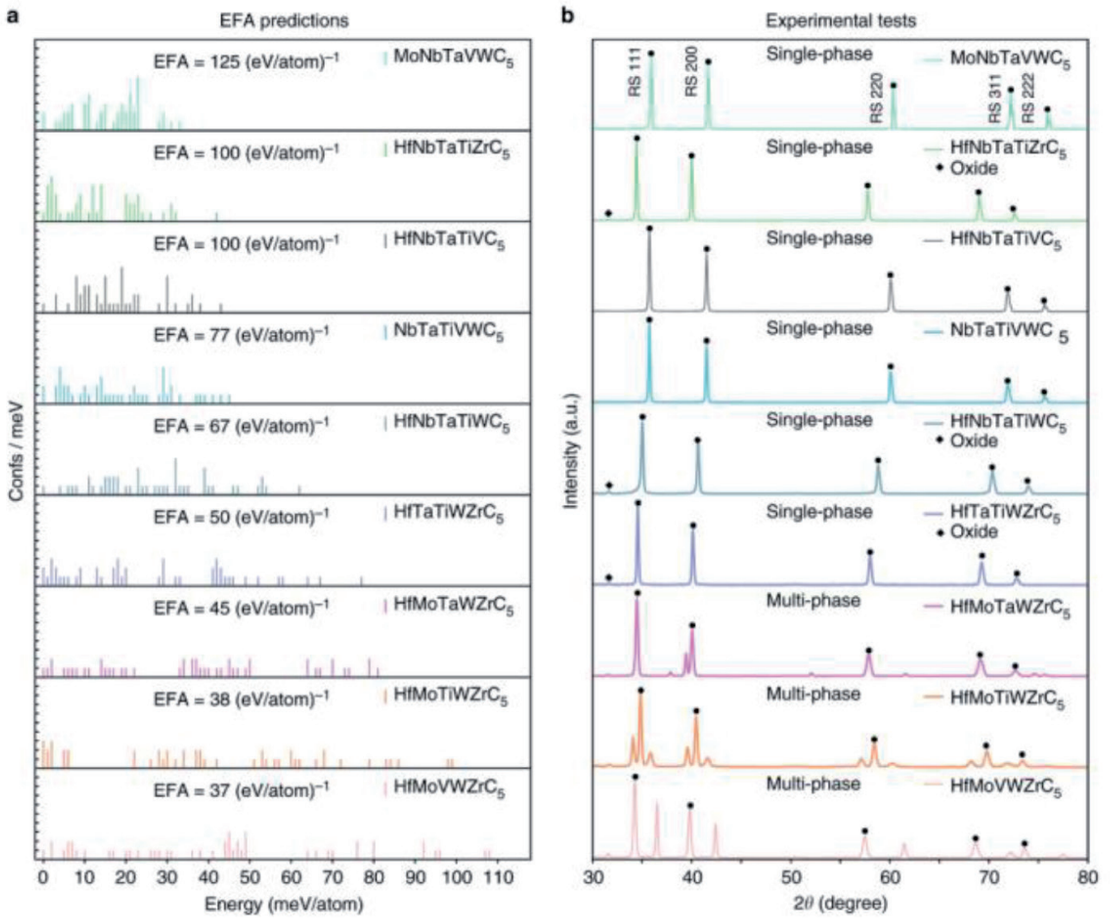

Figure 3.
(a) The energy distribution spectra of different configurations and the corresponding EFA value of the nine five-metal carbides. (b) The X-ray patterns of the sintered carbides with the same compositions, by Sarker et al. [23] (licensed under CC BY 4.0, https://doi.org/10.1038/s41467-018-07160-7).

crystal structures was commonly understood to impede the formation of the high-entropy phase because of the mismatch of lattice structure. It was observed that the addition of group VI elements (Cr, Mo, and W) is likely to reduce the chance of forming a single phase, as group VI metal monocarbides are generally demonstrated as non-cubic structure at room temperature. However, the $MoNbTaVWC_5$ composition that simultaneously contains tungsten carbide (W_2C) and molybdenum carbide (Mo_2C), which exhibit orthorhombic and hexagonal structure, respectively, shows the highest EFA value among the 56 analyzed compositions and demonstrates single-phase FCC structure after SPS. The mechanical properties measured by experiments showed that the Vickers hardness and elastic modulus have significant enhancement compared to the predicted value from the rule of mixture, contributed by mass disorder in the structure and solid solution hardening. Following the work of the pioneers, a systematic study focused on the phase stability and mechanical properties of high-entropy carbides synthesized from group IV, V, and VI metal carbides [25] was carried out. It was verified that carbide system that was stated to have EFA value lower than 45 cannot form single-phase solid solution via SPS.

2.2.4 Other high-entropy ceramics—silicide, borocarbide, sulfide, etc.

To date, the work of bulk high-entropy ceramics is mostly focused on oxide, boride, and carbide, and several other classes of high-entropy materials like silicide, sulfide, and borocarbide have been reported.

The synthesis of high-entropy silicide was reported by Gild et al. [26] and Qin et al. [27]. Gild utilized SPS and sintered high-entropy silicide $(Mo_{0.2}Nb_{0.2}Ta_{0.2}Ti_{0.2}W_{0.2})Si_2$ at 1923 K, resulting in a single hexagonal C40 crystal structure (space group $P6_222$). Hardness enhancement over the constituent silicide and low thermal conductivity similar to high-entropy carbide was reported. On the other hand, Qin produced $(Ti_{0.2}Zr_{0.2}Nb_{0.2}Mo_{0.2}W_{0.2})Si_2$ from compositional elemental powders, leading to the formation of a hexagonal structure high-entropy silicide, with the same space group $P6_222$. Zhang et al. [28] developed a data-driven model to design high-entropy sulfides for thermoelectric applications. Compositions $Cu_5SnMgGeZnS_9$ and $Cu_3SnMgInZnS_7$ were picked to be synthesized via high energy ball milling and SPS. Single-phase high-entropy sulfide with homogeneous distribution of the elements is reported. By increasing the Sn content in the $Cu_5SnMgGeZnS_9$ system, a figure of merit zT value of 0.58 at 773 K was obtained.

By adding B_4C into the four-component HEC (HfMoTaTi)C, Zhang et al. [29] studied the capability of a high-entropy carbide system on accommodating one more nonmetal element, boron. The quaternary (HfMoTaTi)C contains FCC structures, while the addition of B_4C induced the formation of a small fraction of hexagonal phase. Similar with the diffusion process reported by Castle et al. [19], TaC is suggested to act as the host lattice in the borocarbide system. The effect of employing different particle sizes for host carbide TaC and other constituent carbides on the phase formation and mechanical properties of the HEC composites was discussed. A high-entropy $B_4(HfMo_2TaTi)C$ ceramic exhibiting hexagonal structure, with alternating metal and nonmetal layers in the lattice, was found when SiC whiskers are introduced to the borocarbide system [30]. The hexagonal HEC solid solution shows great improvement of the mechanical property with an ultrahigh hardness of 35 GPa.

3. High-entropy ceramic coatings

3.1 Preparation methods

3.1.1 Sputtering

Sputtering is a physical vapor deposition (PVD) technique where a solid surface (target) is bombarded with accelerated charged ions (Ar^+) resulting into backward scattering of surface atoms of solid. Sputtering technique is used to deposit thin coatings. There are several sputtering systems employed for deposition of thin coatings, such as direct current (DC) magnetron sputtering and radio frequency (rf) sputtering being the widely used techniques. DC-magnetron sputtering is a low pressure sputtering system for metal deposition and electrically conductive target coating materials. The magnetic field from magnetron lowers the sputtering gas pressure and increases the deposition rate of sputtered coatings. On the other hand, when metallic target is replaced by an insulator target, the plasma discharge cannot be maintained due to buildup of surface charge of positive ions on the target. Thus, an rf power supply is used instead of dc voltage power supply to sustain the glow discharge on an insulator target [31]. Another advantage of using sputtering for thin coating deposition is the use of reactive gases, substrate bias, and substrate temperature to vary the composition and properties of deposited coatings. In reactive sputtering, different reactive gases, such as oxygen, nitrogen, and CH_4 can be used to deposit ceramic coatings of oxides, nitrides, and carbides, respectively [32–34]. Furthermore, deposition of carbonitride and oxynitride coatings can be

achieved by using a mixture of CH_4 + N_2 and O_2 + N_2, respectively [35, 36]. In reactive sputtering, a mixture of Ar and reactive gas (5–70%) is used for sputtering. The increasing bias between the target and substrate can affect the chemical composite, microstructure, and mechanical properties of the coating by giving compact coating structures. Lastly, substrate temperature can be varied in reactive sputtering to enhance the ion mobility and the interaction between the deposited ions, which can affect the microstructure, composition, and the properties of the coating. The following section will be used to highlight the use of reactive sputtering to deposit high-entropy nitride, carbide, and oxide ceramic coatings.

3.2 Structural evolution

3.2.1 High-entropy nitride coatings

High-entropy alloys based on multi-principle elements make it possible to design various nitride coatings. The use of nitride forming multi-principle elements can enhance the physical and mechanical properties that are not achievable in the conventional binary- and ternary-nitride coatings [37]. The high-entropy nitride coatings form amorphous and/or solid solution with face-centered cubic (FCC) structure. The severe lattice distortion and solid solution hardening help in developing high strength nitride coatings for various applications that require wear resistance, corrosion resistance, diffusion barrier, electrical resistivity, biocompatibility or light reflectivity [38]. The versatile sputtering deposition can be used to vary the N_2 flow, substrate temperature, and substrate bias to obtain nitride coatings with good physical, chemical, and mechanical properties, respectively.

3.2.2 Effect of N_2 flow rate

The high-entropy nitride (HEN) coatings developed by DC-magnetron sputtering were reported by research group of Yeh et al. using targets of FeCoNiCrCuAlMn, FeCoNiCrCuAl, AlxCoCrCuFeNi (x: 0.5 and 2), and AlCrNiSiTi [39]. In all the cases, the resulting HEN coatings showed formation of FCC solid solution at low N_2 flow rate (R_N) and became amorphous at higher N_2 flow rate (R_N) due to severe lattice distortion and presence of weak nitride forming elements, such as Al and Si, where $R_N = (N_2/(Ar + N_2))$. Following this work, Lai et al. developed (AlCrTaTiZr)N HEN coating, where the coating structure changed from amorphous phase metallic coating to FCC solid solution HEN with increasing N_2 flow rate [32]. The sputtering rate decreased from 35 nm/min (R_N = 0%) to 15 nm/min (R_N = 60%) with increasing N_2 flow ratio (R_N). The decreasing sputtering rate was attributed to a lower sputtering yield due to nitrogen absorption, nitridation of the target, and/or decreasing sputtering efficiency of reactive gases with increasing R_N as compared to argon ions. The increasing R_N ratio resulted in increasing the hardness from 9 GPa (0% R_N) to 32 GPa (15% R_N). In another study, Tsai et al. developed octonary principal element (AlMoNbSiTaTiVZr)N HEN coatings using magnetron sputtering with nitrogen flow ratio from 0 to 70% R_N [40]. The deposition rate decreased from 31 nm/min (R_N = 0%) to 8.3 nm/min (R_N = 67%) with increasing nitrogen flow ratio. In contrast, the hardness values increased from 13.5 GPa (0% R_N) to 37 GPa (50% R_N). Such high increase in hardness has been attributed to the stronger bonding between N and target elements. The coating morphology of (AlMoNbSiTaTiVZr)N HEN changed from coarser grain-like morphology (R_N = 0%; grain size: 30–100 nm) to reduced grain morphology (R_N = 11%; grain size: 10 nm) and then to rougher morphology (R_N = 33%). Similarly, the cross-section of the coating changed from a glass-like

featureless morphology to fine columnar structure with increasing nitrogen flow ratio from R_N = 0–11% to R_N = 33%, respectively. Similarly, Xing et al. developed (NbTiAlSiZr)N HEN coating using RF sputtering with increasing nitrogen flow rate from 10 to 50% [41]. The coating thickness and deposition rate were found to decrease with increasing nitrogen flow rate, as shown in **Figure 4**.

The cross-section of (NbTiAlSiZr)N HEN coatings is shown in **Figure 5**. The coating thickness was found to decrease from 298.8 to 200 nm with increasing nitrogen flow rate. Furthermore, the hardness was found to increase from 9.5 to 12 GPa with the increasing nitrogen flow rate of R_N = 10% to R_N = 50%, respectively.

In another work, Chang developed a duodenary (TiVCrZrNbMoHfTaWAlSi)N HEN coatings with R_N from 0 to 50% using DC magnetron sputtering and similar structural evolution from amorphous to FCC solid solution was observed with increasing R_N [42]. The hardness after reactive sputtering increased from 13 GPa (0% R_N) to 34.8 GPa (50% R_N).

3.2.3 Effect of substrate bias

The changing substrate bias during coating deposition effects the chemical composition, microstructure, and mechanical properties of coatings. Chang et al. studied the effect of substrate bias from 0 to −200 V on (AlCrMoSiTi)N HEN coatings developed by DC magnetron sputtering at 50% R_N [43]. The coating showed FCC solid solution structure even though it contained immiscible nitrides, such as AlN, TiN, and Si_3N_4. However, the lattice parameter increased from 4.15 to 4.25 Å, and the grain size decreased from 16.8 to 3.3 nm with increasing substrate bias. This change in the lattice parameter was attributed to increase in adatom mobility, and the decreasing grain was due to increase in nucleation rate at ion-induced surface defects with changing substrate bias. The increasing substrate bias had a small effect on the hardness properties from 25 GPa with no bias to highest hardness of 32 GPa observed at −100 V bias. Following these findings, Huang et al. studied the effect of increasing substrate bias from 0 to −160 V on (AlCrNbSiTiV)N HEN coating using RF magnetron sputtering with R_N and substrate temperature kept constant at 28% and 300°C, respectively [44]. The XRD analysis of HEN coatings

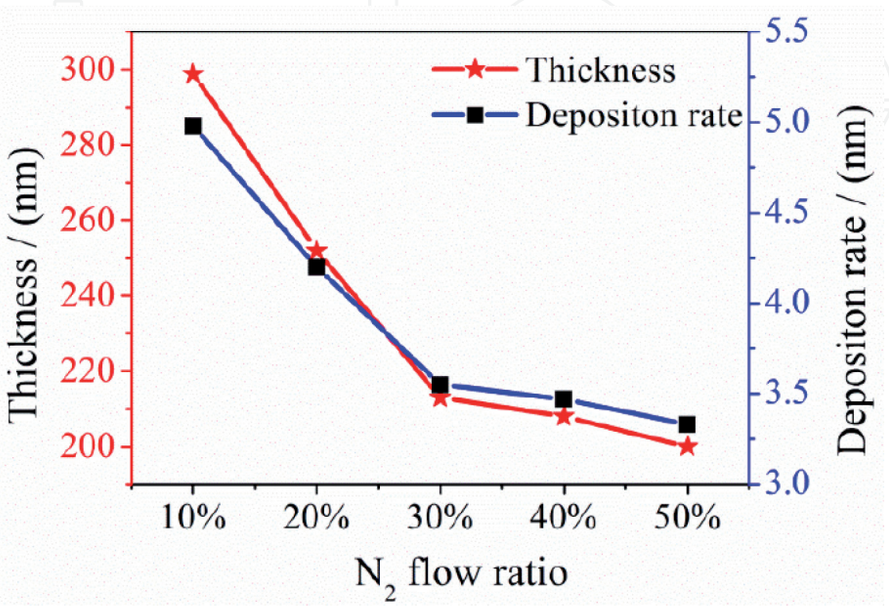

Figure 4.
Film deposition rate as a function of nitrogen flow ratio (R_N) in (NbTiAlSiZr)N HEN coatings [41].

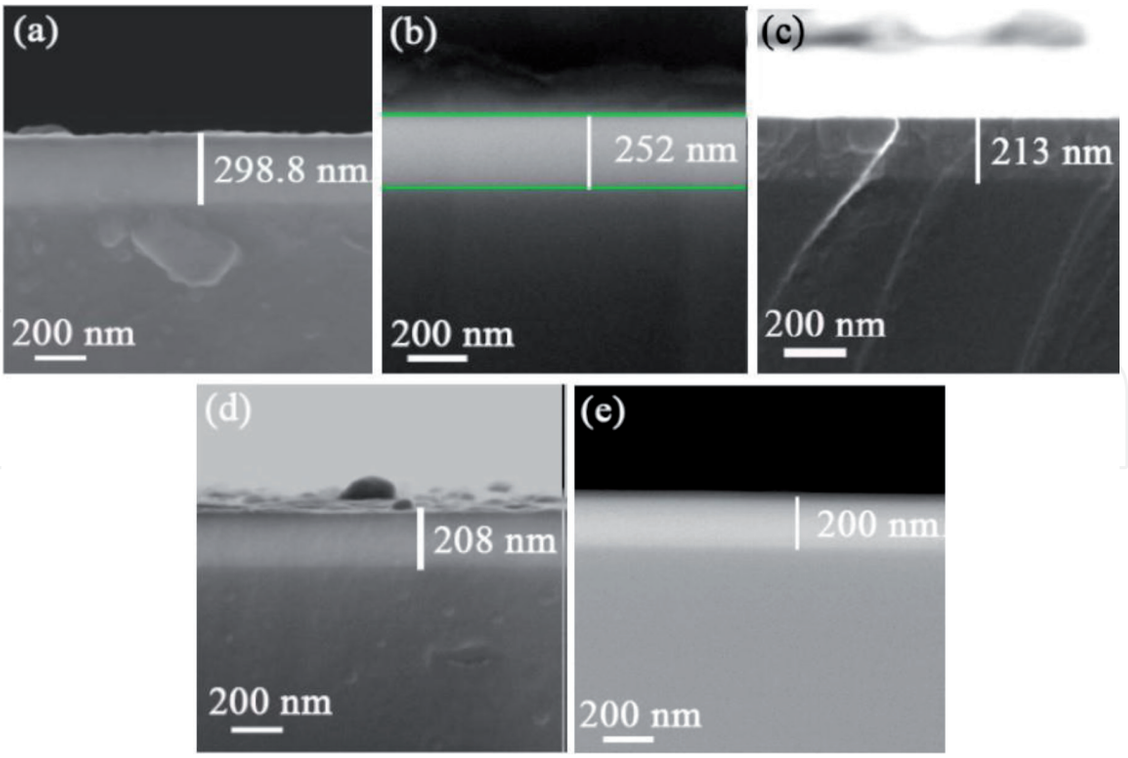

Figure 5.
Surface and cross-section SEM micrographs of (NbTiAlSiZr)N HEN coatings at various R_N: (a) R_N = 10%, (b) R_N = 20%, (c) R_N = 30%, (d) R_N = 40%, and (e) R_N = 50% [41].

showed FCC solid solution with a similar increasing and decreasing trends of lattice parameters and grain size, respectively. However, in this work, the hardness increased from 22 GPa with no bias to the highest hardness of 42 GPa achieved at −100 V bias. The (AlCrNbSiTiV)N HEN coating showed excellent thermal stability even after annealing at 800°C (5 h) and maintained a hardness of 40 GPa. Such increasing trend in hardness was attributed to changing grain size and residual stress with increasing substrate bias. Similar effect of substrate bias on the coating structure and properties were observed in (TiVCrZrHf)N [45], (AlCrTaTiZr)N [46], (TiHfZrVNb)N [47], and (TiZrHfNbTaY)N [48] HEN coatings.

3.2.4 Effect of substrate temperature

The growth of film during the deposition in sputtering system is dependent on the mobility of ions to the substrate. The substrate temperature can play a key role toward ion mobility and diffusion between deposited ions that affect the microstructure, composition, and properties of the coatings. Liang et al. investigated the effect of substrate temperature on the deposition of (TiVCrZrHf)N HEN coating using RF magnetron sputtering from room temperature (RT; 25°C) to 450°C with a fixed 4% R_N and −100 V substrate bias [49]. The XRD analysis showed formation of FCC solid solution without any significant phase separation at all substrate temperatures. However, grain size decreased from 10.7 nm at RT to 8 nm at 250°C and then increased to 9.7 nm at 450°C. The surface morphology of (TiVCrZrHf)N HEN coating became more smooth and dense with increasing substrate temperature. The cross-section morphology changed from an amorphous phase at coating-substrate interface to FCC phase toward coating surface. This phenomenon was reported to be due to higher stresses generated in the initial coating deposition and the greater lattice mismatch of 19% between the HEN coating and silicon substrate. The hardness of the coating increased from 30 to 48 GPa with increasing substrate

temperature from RT to 450°C. The high hardness with increasing substrate temperature was attributed to the higher mobility of deposited atoms and reduction of growth void leading to denser coatings. Similar studies on the effect of substrate temperature on structure and enhancement of mechanical properties were studied on the deposition of (AlCrNbSiTiV)N [50–52] and (TiVCrAlZr)N [53] HEN coating.

3.3 High-entropy carbide coatings

Similar to high-entropy nitride coatings, high-entropy carbide coatings have been developed to obtain coatings for tribological and biomedical applications.

3.3.1 Effect of CH_4 flow rate ratio

Braic et al. performed the initial studies on development of high-entropy carbide coatings for tribological and biomedical applications. Their research group deposited (TiAlCrNbY)C high-entropy carbide coatings from co-sputtering of elemental targets using DC-magnetron sputtering with different CH_4 flow ratios (R_C), and at constant substrate temperature and substrate bias of 400°C and −100 V, respectively [54], where CH_4 flow ratio is given by: $R_C = CH_4/(CH_4 + Ar)$. The XRD data showed a change of structure from nanostructured broad FCC phase (0% R_C) to a single FCC carbide phase (10 and 17% R_C) and then to amorphous phase at higher carbon concentration (26 and 33% R_C). The coating morphology changed from slightly higher surface roughness of 7 nm (0% R_C) to fine grained surface roughness of 2 nm (33% R_C) with increasing CH_4 flow ratio. The hardness values increased from 8.2 GPa (0% R_C) to 22.6 GPa (26% R_C). Similarly, Braic et al. studied the effect of CH_4 flow ratio on (TiZrNbHfTa)C high-entropy carbide coating with elemental target co-sputtering using DC-magnetron sputtering on Ti6Al4V alloy substrate [55]. However, in this work, formation of only FCC solid solution was observed at R_C of 13 and 35% with hardness values of 22.4 and 32.1 GPa, respectively. Similar to earlier work, the surface roughness and crystallite size decreased, while the hardness increased with increasing CH_4 flow ratio. In another work, Braic et al. deposited (CuSiTiYZr)C high-entropy carbide coating using elements with large atomic radii differences and reported the effect of different CH_4 flow ratios on the structural and mechanical properties. In all the deposited high-entropy carbide coatings, the XRD showed the formation of amorphous phase irrespective of the amount of carbon. The higher lattice distortion in the high-entropy carbide coatings resulted in hardness values of 20.7 GPa (25% R_C), 27.2 GPa (35% R_C), and 29.5 GPa (50% R_C). Thus, proving the work of Zhang et al. [56] and Guo et al. [57] in the case of high-entropy alloys, a solid solution is formed when the constituent elements have a close atomic radius. Similarly, Jhong et al. developed (CrNbSiTiZr)C high-entropy carbide coatings and studied the effect of increasing CH_4 flow ratio on the structural evolution and mechanical properties [58]. In this system, the structure of high-entropy carbide coating changed from FCC solid solution phase at lower R_C of 3–10% to amorphous phase at higher R_C of 15–20%. Such structural change from FCC to amorphous phase resulted in reducing the hardness from 32.8 to 22.3 GPa.

3.3.2 Effect of substrate temperature

Braic et al. studied the effect of substrate temperature on the deposition of (CrCuNbTiY)C high-entropy carbide coating with DC co-sputtering of elemental targets with a constant substrate bias and two different CH_4 flow ratios. The substrate temperature was increased from 80 to 650°C, and its effect on the structural

evolution and mechanical properties were reported. The high-entropy carbide coating with lower carbon concentration showed formation of FCC structures at all the deposition temperatures, while the coating with higher carbon concentration showed poor crystallinity and approaching toward an amorphous phase. The grain size and surface roughness increased with increasing substrate temperature in both coatings. In contrast, the hardness values increased with increasing substrate temperature from 13 GPa (80°C substrate temperature) to 30 GPa (650°C).

3.4 High-entropy oxide coatings

Most of the research on high-entropy ceramic coatings has been focused on high-entropy nitrides and carbide coatings. Few research works have been reported on high-entropy oxide (HEO) coatings. Initial work on HEO coatings was reported by Chen and Wong, where $(Al_xCoCrCuFeNi)O$ (x: 0.5, 1 or 2) HEO coating by RF magnetron sputtering using different oxygen flow ratios (O_2/Ar) was developed, and the resulting structural evolution was characterized [59]. The structural evolution was observed to change from FCC, FCC + BCC or BCC (depending on the amount of Al content) to cubic spinal oxides with increasing oxygen flow ratio. The hardness increased from 5–8 GPa to 13–22.6 GPa with increasing O_2 flow ratio. In a subsequent work, Lin et al. used strong oxide forming elements to develop (AlCrTaTiZr)O HEO coating using DC magnetron sputtering with increasing O_2 flow ratio ($R_O = O_2/(O_2 + Ar)$) from 0 to 50%. The XRD analysis revealed a metastable amorphous structure irrespective of the O_2 flow ratio [33]. The tendency of forming amorphous phases at different O_2 flow ratios has been attributed to the large difference in the lattice parameters of oxides from each constituent element of Al, Cr, Ta, Ti, and Zr. The hardness values were reported to be in the range of 8–13 GPa. However, the hardness values increased in the range of 20–22 GPa after annealing at 900°C. The reported hardness values of HEO coatings were relatively higher than most of the reported oxide films, such as Al_2O_3 (10 GPa) [60], TiO_2 (18 GPa) [61], V_2O_5 (3–7 GPa) [62], and ZrO_2 (15 GPa) [63].

3.5 Properties of high-entropy ceramic coatings

3.5.1 Mechanical properties

Based on the reported high-entropy nitride (HEN) coatings in literature, it can be seen that the hardness of HEN coating is dependent on the selection of element that are strong nitride formers in multicomponent alloy. In the earlier work on (FeCoNiCrCuAlMn)N and $(FeCoNiCrCuAl_{0.5})N$ HEN coatings, a maximum hardness of 10.4–11.8 GPa was observed at higher N_2 flow ratio [39]. Consequently, HEN coatings containing strong nitride forming elements, such as (AlCrNbSiTiV)N [44], (TiVCrZrHf)N [49], and (TiZrNbAlYCr)N [64], were developed resulting in hardness increase of 40–48 GPa with increasing N_2 flow ratio. Furthermore, the mechanical properties have been found to increase with increasing substrate-bias and temperature. Some of the HEN coatings reported in literature with superior mechanical properties have been summarized in **Table 1**.

3.5.2 Tribological properties

The superior mechanical properties and high temperature stability of high-entropy nitride (HEN) and high-entropy carbide coating make them suitable toward tribological applications. Few research works have been reported on tribological studies of HEN and high-entropy carbide coating as a function of N_2/

HEN coating	Max. hardness (GPa)	Max. Young's modulus (GPa)	Ref.
(AlCrTaTiZr)N	32	368	[32]
(AlCrMoSiTi)N	35	325	[43]
(AlMoNbSiTaTiVZr)N	37	360	[65]
(AlCrNbSiTiV)N	42	350	[66]
(TiVCrZrHf)N	48	316	[67]
(TiZrNbHfTa)N	32.9	—	[68]
(TiVCrZrHf)N	33	276	[45]
(AlCrNbSiTi)N	36.7	425	[69]
(TiHfZrVNb)N	44.3	—	[47]
(AlCrMoTaTi)N	30.6	280	[70]
(AlCrMoTaTiSi)N	36	250	[71]
(TiVCrZrNbMoHfTa-WAlSi)N	34.8	276.5	[42]
(TiZrNbAlYCr)N	47	—	[64]
(TiZrHfNbTaY)N	40.2	—	[48]

Table 1.
Mechanical properties of high-entropy nitride coatings.

CH_4 gas flow ratio and substrate bias. Lai et al. studied the effect of substrate bias on tribological properties of (AlCrTaTiZr)N HEN coatings against steel counter ball [46]. The resulting wear test showed a high COF of 0.7, while the wear rate decreased from 6.4×10^{-6} to 3.6×10^{-6} mm^3/Nm with increasing substrate bias. The (AlCrTaTiZr)N HEN coating was found to be stable after the wear test of 70 m sliding distance. In another work, Cheng et al. studied the effect of N_2 flow rate on tribological properties of (AlCrMoTaTiZr)N HEN coatings against steel counter ball for a sliding distance of 90 m [72]. The resulting tribological test showed a low wear rate of 2.8×10^{-6} mm^3/Nm; however, the COF was found to be still high around 0.7. Similarly, Braic et al. studied the tribological behavior of (TiZrNbHfTa)N HEN coating and (TiZrNBHfTa)C high-entropy carbide coating on M2 steel substrate against sapphire counter ball for a sliding distance of 400 m at ambient conditions [68]. The wear test showed an average COF of 0.9 and an average wear rate of 2.9×10^{-6} mm^3/Nm for (TiZrNbHfTa)N HEN coating, and an average COF of 0.15 and an average wear rate of 8×10^{-7} mm^3/Nm for (TiZrNbHfTa)C high-entropy carbide coating. Following this work, wear test of (TiZrNbHfTa)N HEN coating and (TiZrNBHfTa)C high-entropy carbide coating was carried out in simulated body fluid (SBF) against sapphire counter ball for a sliding distance of 400 m [55]. The resulting wear test showed an average COF and wear rate of 0.17 and 2.9×10^{-7} mm^3/Nm for (TiZrNbHfTa)N HEN coating and an average COF and wear rate of 0.12–0.32 and 2–9 $\times 10^{-7}$ mm^3/Nm for (TiZrNbHfTa)C high-entropy carbide coating, respectively. Furthermore, Braic et al. and Jhong et al. studied the tribological performance of (TiAlCrNbY)C [54], (CuSiTiYZr)C [34], (CrCuNbTiY)C [73], and (CrNbSiTiZr)C [58] high-entropy carbide coatings and showed high-entropy carbide coating possessing superior tribological properties with wear rate and COF values in the range of 0.12–12 $\times 10^{-6}$ mm^3/Nm and 0.07–0.4, respectively.

Following the initial works on ball-on-disc sliding wear tests on HEN coatings, simulated tests have been performed for cutting tools application. Shen et al. studied the milling performance of (AlCrNbSiTi)N HEN coated WC-Co substrate

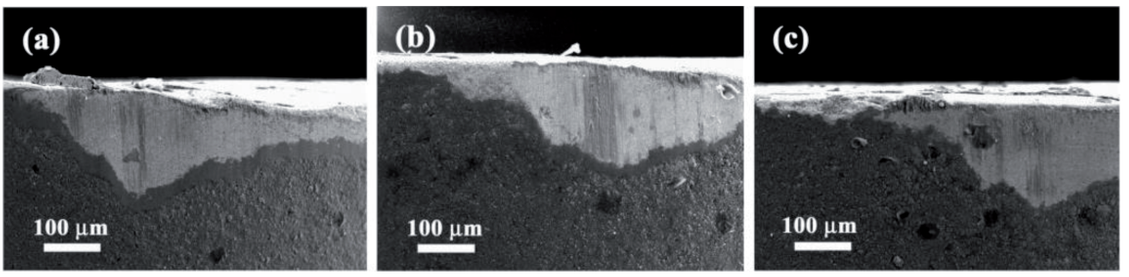

Figure 6.
SEM micrographs of flank wear morphology of cutting inserts coated with: (a) TiN, (b) TiAlN, and (c) AlCrNbSiTi HEN coating [74] (licensed under CC BY 4.0, DOI: 10.3390/coatings5030312).

against SKD11 steel for a sliding distance of 900 m and compared its performance to commercial TiN and TiAlN coatings [74]. The resulting milling tests showed a lower flank wear of 200 μm/min for (AlCrNbSiTi)N HEN coating as compared to 255 μm/min in TiN and 270 μm/min in TiAlN, as shown in **Figure 6**. Similarly, machining performance of (TiZrHfVNbTa)N [75], (AlCrNbSiTiV)N [51], and nanolaminate (TiAlCrSiY)N/(TiAlCr)N [76] HEN coatings showed better tribological properties than commercial nitride coatings.

3.5.3 Corrosion properties

The increase in lattice distortion with high number of principle elements results in formation of amorphous phase in high-entropy alloys, which in return gives better mechanical and electrochemical properties. The corrosion resistance of conventional alloys can be enhanced with amorphous HEA coatings by choosing the appropriate chemical compositions. Lin deposited (TiAlCrSiV)N HEN coatings on a mild steel substrate at different R_N flow ratios and studied its electrochemical properties in 3.5 wt.% NaCl solution at room temperature (RT; 22°C). The coating structure changed from amorphous phase at lower R_N flow ratio to FCC solid solution at higher R_N flow ratio. The highest polarization resistance of 11.36 kΩ/cm^2 was observed in the metallic TiAlCrSiV HEA coating, while the polarization resistance slightly decreased to 8.03–8.55 kΩ/cm^2 in its nitride coatings. Furthermore, the polarization resistance of HEN coatings was enhanced by developing an interlayer of metallic TiAlCrSiV HEA coating. In another work, Hsueh et al. deposited (AlCrSiTiZr)N HEN coating on 6061 aluminum alloy and mild steel substrates using DC magnetron sputtering at various R_N flow ratios, and studied the effect of R_N flow ratio and substrate bias during deposition on corrosion properties in 0.1 M H_2SO_4 aqueous solution at RT [77]. The (AlCrSiTiZr)N HEN coating changed from an amorphous structure to partially crystalline structure at higher R_N flow ratios. The resulting corrosion current density (i_{corr}) for 6061 aluminum alloy substrate decreased from 29.1 μA/cm^2 (uncoated) to 3.1 μA/cm^2 with (AlCrSiTiZr)N HEN coating; while for mild steel substrate, it decreased from 90.4 μA/cm^2 (uncoated) to 7.7 μA/cm^2. Similar increase in corrosion/oxidation resistance with HEN coating on conventional substrate was observed in (TiZrNbHfTa)N and (TiZrNbHfTa)C [55], (AlCrNbSiTi)N [69], nanolaminated AlCrMoNBZr/(AlCrMoNbZr)N [76, 78], and (NbTiAlSiZr)N [41] HEN coating.

4. Future possibility and commercialization

As compared to high-entropy alloys, fewer reports have been published on crystalline high-entropy ceramics (HECs). Due to the high melting point, high hardness, and good thermal and chemical stability, as well as excellent wear and

oxidation resistance of ceramic materials, most of the bulk HECs such as high-entropy borides and carbides are designed to be the new type of ultra-high-temperature ceramics (UHTC) with increased high-temperature stability and superior mechanical properties over conventional ceramics. The current understanding of processing and evolution of properties of bulk HECs was built on and developed from the knowledge of HEAs. For bulk HECs, the preferred ceramic components are group IV, V, and VI metal ceramics (metal boride, carbide, silicide, etc.) due to their closely matched structure and properties. Compared to metallic HEAs system where only elemental materials are used, the combination of HEC composition is greatly limited. More experimental efforts on screening and investigation of HECs with different compositions are required to explore the potential of HECs. Furthermore, most of the reported bulk HECs is based on experimental observations, while a few are systematically discussed in combination with the modeling results. In order to give future researchers a clear guideline of designing HECs, further development on computational methods including corresponded thermodynamic ceramic database is needed to more effectively and accurately predict the structure and properties of HECs.

The research on the processing of HECs is progressing, and there have been considerable work performed in the industry on the coatings of HECs toward the next generation of nitride and carbide coatings. High-entropy carbide and nitride coatings have potential applications in biomedical industry, cutting tools, and hard facing die coatings due to their superior mechanical, corrosion, and oxidation resistant properties [55, 74]. HEC coatings of nitride with high thermal stability can be applied as diffusion barrier coatings in integrated circuits to inhibit the diffusion of adjacent materials (e.g., Cu and Si) [79]. Furthermore, high-entropy oxide coatings can be considered as a potential future material for cuprate superconductors, visible-light photocatalysts, and transparent field-effect transistors (TFETs) [59].

5. Summary

Researches of bulk high-entropy ceramic have been reported on metal oxides, refractory carbides, borides, and silicides. HECs with homogenous single-phase structure reveal superior mechanical performance and additional properties like thermal-electrical property of high-entropy oxides. Most scientific effort has been put in exploring various fabrication methods, characterizing the high-entropy structure and the remarkable physical and chemical properties. However, to fully understand HECs that involves a complex multicomponent ceramic system, the problem remains: what are the most significant phase formation rules in a HECs material? How can the potential applications of HECs be realized? A more systematic investigation of the material selection rules that already exists in a metallic high-entropy system is highly demanded in the ceramic system in order to optimize the material design and processing work.

The reported research in the past 10 years on high-entropy ceramic coatings has shown development of coatings with exceptional mechanical, high temperature, electrical, corrosion, and wear-resistant properties. High-entropy ceramic coatings have great potential in different applications, such as wear and corrosion resistant coatings, thermal barrier coatings, and electrical and biomedical applications. The control on variation of deposition parameters can be advantageous in achieving coating with extremely high strength values and highly densified structures, which can be corrosion resistant and biocompatible. Future work on development of nanocomposite and multilayer high-entropy ceramic coatings

can possess super hardness properties. Furthermore, high temperature corrosion, mechanical, and tribological properties of high-entropy ceramic coatings need to be addressed.

Author details

Sajid Ali Alvi, Hanzhu Zhang and Farid Akhtar*
Division of Materials Science, Luleå University of Technology, Luleå, Sweden

*Address all correspondence to: farid.akhtar@ltu.se

References

[1] Feng L, Fahrenholtz WG, Hilmas GE, Zhou Y. Synthesis of single-phase high-entropy carbide powders. Scripta Materialia. 2019;**162**:90-93

[2] Ye B, Ning S, Liu D, Wen T, Chu Y. One-step synthesis of coral-like high-entropy metal carbide powders. Journal of the American Ceramic Society. 2019:jace.16514. 2019;**102**:6372-6378

[3] Liu D, Wen T, Ye B, Chu Y. Synthesis of superfine high-entropy metal diboride powders. Scripta Materialia. 2019;**167**:110-114

[4] Zhang AY, Jiang Z, Sun S, Chen Q, Qiu J, Plucknett K. Microstructure and mechanical properties of high-entropy borides derived from boro/carbothermal reduction. Journal of the European Ceramic Society. 2019;**39**(13):3920-3924

[5] Wei X-FF, Liu J-XX, Li F, Qin Y, Liang Y-CC, Zhang G-JJ. High entropy carbide ceramics from different starting materials. Journal of the European Ceramic Society. 2019;**39**(10):2989-2994

[6] Rost CM, Sachet E, Borman T, Moballegh A, Dickey EC, Hou D, et al. Entropy-stabilized oxides. Nature Communications. 2015;**6**:8485

[7] Rost CM, Rak Z, Brenner DW, Maria JP. Local structure of the MgxNixCoxCuxZnxO(x=0.2) entropy-stabilized oxide: An EXAFS study. Journal of the American Ceramic Society. 2017;**100**(6):2732-2738

[8] Anand G, Wynn AP, Handley CM, Freeman CL. Phase stability and distortion in high-entropy oxides. Acta Materialia. 2018;**146**:119-125

[9] Bérardan D, Franger S, Dragoe D, Meena AK, Dragoe N. Colossal dielectric constant in high entropy oxides. Physica Status Solidi Rapid Research Letters. 2016;**10**(4):328-333

[10] Bérardan D, Franger S, Meena AK, Dragoe N. Room temperature lithium superionic conductivity in high entropy oxides. Journal of Materials Chemistry A. 2016;**4**(24):9536-9541

[11] Sarkar A, Velasco L, Wang D, Wang Q, Talasila G, de Biasi L, et al. High entropy oxides for reversible energy storage. Nature Communications. 2018;**9**(1):3400

[12] Jiang S, Hu T, Gild J, Zhou N, Nie J, Qin M, et al. A new class of high-entropy perovskite oxides. Scripta Materialia. 2018;**142**:116-120

[13] Djenadic R, Sarkar A, Clemens O, Loho C, Botros M, Chakravadhanula VSK, et al. Multicomponent equiatomic rare earth oxides. Materials Research Letters. 2017;**5**(2):102-109

[14] Gild J, Samiee M, Braun JL, Harrington T, Vega H, Hopkins PE, et al. High-entropy fluorite oxides. Journal of the European Ceramic Society. 2018;**38**(10):3578-3584

[15] Gild J, Zhang Y, Harrington T, Jiang S, Hu T, Quinn MC, et al. High-entropy metal diborides: A new class of high-entropy materials and a new type of ultrahigh temperature ceramics. Scientific Reports. 2016;**6**:2-11

[16] Sarkar A, Velasco L, Wang D, Wang Q, Talasila G, de Biasi L, et al. Ab initio prediction of mechanical and electronic properties of ultrahigh temperature high-entropy ceramics ($Hf_{0.2}Zr_{0.2}Ta_{0.2}M_{0.2}Ti_{0.2})B_2$ (M = Nb, Mo, Cr). Scripta Materialia. 2018;**9**(8):328-333

[17] Tallarita G, Licheri R, Garroni S, Orrù R, Cao G. Novel processing route for the fabrication of bulk high-entropy metal diborides. Scripta Materialia. 2019;**158**:100-104

[18] Zhang Y, Guo WM, Bin JZ, Zhu QQ, Sun SK, You Y, et al. Dense

high-entropy boride ceramics with ultra-high hardness. Scripta Materialia. 2019;**164**:135-139

[19] Castle E, Csanádi T, Grasso S, Dusza J, Reece M. Processing and properties of high-entropy ultra-high temperature carbides. Scientific Reports. 2018;**8**(1):1-12

[20] Dusza J, Švec P, Girman V, Sedlák R, Castle EG, Csanádi T, et al. Microstructure of (Hf-Ta-Zr-Nb)C high-entropy carbide at micro and nano/atomic level. Journal of the European Ceramic Society. 2018;**38**(12):4303-4307

[21] Yan X, Constantin L, Lu Y, Silvain JF, Nastasi M, Cui B. $(Hf_{0.2}Zr_{0.2}Ta_{0.2}Nb_{0.2}Ti_{0.2})C$ high-entropy ceramics with low thermal conductivity. Journal of the American Ceramic Society. 2018;**101**(10):4486-4491

[22] Zhou J, Zhang J, Zhang F, Niu B, Lei L, Wang W. High-entropy carbide: A novel class of multicomponent ceramics. Ceramics International. 2018;**44**(17):22014-22018

[23] Sarker P, Harrington T, Toher C, Oses C, Samiee M, Maria J-PP, et al. High-entropy high-hardness metal carbides discovered by entropy descriptors. Nature Communications. 2018;**9**(1):4980

[24] Yang K, Oses C, Curtarolo S. Modeling off-stoichiometry materials with a high-throughput ab-initio approach. Chemistry of Materials. 2016;**28**(18):6484-6492

[25] Harrington TJ, Gild J, Sarker P, Toher C, Rost CM, Dippo OF, et al. Phase stability and mechanical properties of novel high entropy transition metal carbides. Acta Materialia. 2019;**166**:271-280

[26] Gild J, Braun J, Kaufmann K, Marin E, Harrington T, Hopkins P, et al. A high-entropy silicide: $(Mo_{0.2}Nb_{0.2}Ta_{0.2}Ti_{0.2}W_{0.2})Si_2$. Journal of Materiomics. 2019;**5**(3):337-343

[27] Qin Y, Liu J-X, Li F, Wei X, Wu H, Zhang G-J. A high entropy silicide by reactive spark plasma sintering. Journal of Advanced Ceramics. 2019;**8**(1):148-152

[28] Zhang R, Gucci F, Zhu H, Chen K, Reece MJ. Data-driven design of ecofriendly thermoelectric high-entropy sulfides. 2018;**57**(20):13027-13033

[29] Zhang H, Akhtar F. Processing and characterization of refractory quaternary and quinary high-entropy carbide composite. Entropy. 2019;**21**(5):474

[30] Zhang H, Hedman D, Feng P, Han G, Akhtar F, Akhta F. A high-entropy B4$(HfMo_2TaTi)C$ and SiC ceramic composite. Dalton Transactions. 2019;**48**:5161-5167

[31] Wasa K. Fundamentals and applications for functional thin films. In: Handbook of Sputter Deposition Technology. Elsevier; 2012. 660 p

[32] Lai CH, Lin SJ, Yeh JW, Chang SY. Preparation and characterization of AlCrTaTiZr multi-element nitride coatings. Surface and Coatings Technology. 2006;**201**(6):3275-3280. DOI: 10.1016/j.surfcoat.2006.06.048

[33] Lin MI, Tsai MH, Shen WJ, Yeh JW. Evolution of structure and properties of multi-component $(AlCrTaTiZr)ox$ films. Thin Solid Films. 2010;**518**(10):2732-2737. DOI: 10.1016/j.tsf.2009.10.142

[34] Braic M, Balaceanu M, Vladescu A, Zoita CN, Braic V. Deposition and characterization of multi-principal-element $(CuSiTiYZr)C$ coatings. Applied Surface Science. 2013;**284**:671-678. DOI: 10.1016/j.apsusc.2013.07.152

[35] Lv CF, Zhang GF, Cao BS, He YY, Hou XD, Song ZX. Structure and mechanical properties of a-C/(AlCrWTaTiNb)CxNy composite films. Surface Engineering. 2016;**32**(7):541-546

[36] Yu R, Huang R, Lee C, Shieu F. Synthesis and characterization of multi-element oxynitride semiconductor film prepared by reactive sputtering deposition. Applied Surface Science. 2012;**263**:58-61

[37] Li W, Liu P, Liaw PK. Microstructures and properties of high-entropy alloy films and coatings: A review. Materials Research Letters. 2018;**6**(4):199-229. DOI: 10.1080/21663831.2018.1434248

[38] Yeh JW, Chen YL, Lin SJ, Chen SK. High-entropy alloys—A new era of exploitation. Materials Science Forum. 2007;**560**:1-9

[39] Chen TK, Wong MS, Shun TT, Yeh JW. Nanostructured nitride films of multi-element high-entropy alloys by reactive DC sputtering. Surface and Coatings Technology. 2005;**200**(5-6):1361-1365

[40] Tsai MH, Lai CH, Yeh JW, Gan JY. Effects of nitrogen flow ratio on the structure and properties of reactively sputtered (AlMoNbSiTaTiVZr)Nx coatings. Journal of Physics D: Applied Physics. 2008;**41**(23)

[41] Xing Q, Wang H, Chen M, Chen Z, Li R, Jin P, et al. Mechanical properties and corrosion resistance of NbTiAlSiZrNx high-entropy films prepared by RF magnetron sputtering. Entropy. 2019;**21**:396

[42] Chang Z. Structure and properties of duodenary (TiVCrZrNbMoHfTaWAlSi)N coatings by reactive magnetron sputtering. Materials Chemistry and Physics. 2018;**220**:98-110. DOI: 10.1016/j.matchemphys.2018.08.068

[43] Chang HW, Huang PK, Yeh JW, Davison A, Tsau CH, Yang CC. Influence of substrate bias, deposition temperature and post-deposition annealing on the structure and properties of multi-principal-component (AlCrMoSiTi)N coatings. Surface and Coatings Technology. 2008;**202**(14):3360-3366

[44] Huang P-K, Yeh J-W. Effects of substrate bias on structure and mechanical properties of (AlCrNbSiTiV)N coatings. Journal of Physics D: Applied Physics. 2009;**42**(11):115401. Available from: http://stacks.iop.org/0022-3727/42/i=11/a=115401?key=crossref.6aa81f793403c9956100753c5880ec88

[45] Tsai DC, Liang SC, Chang ZC, Lin TN, Shiao MH, Shieu FS. Effects of substrate bias on structure and mechanical properties of (TiVCrZrHf)N coatings. Surface and Coatings Technology. 2012;**207**:293-299. DOI: 10.1016/j.surfcoat.2012.07.004

[46] Lai CH, Cheng KH, Lin SJ, Yeh JW. Mechanical and tribological properties of multi-element (AlCrTaTiZr)N coatings. Surface and Coatings Technology. 2008;**202**(15):3732-3738

[47] Pogrebnjak AD, Yakushchenko IV, Bagdasaryan AA, Bondar OV, Krause-Rehberg R, Abadias G, et al. Microstructure, physical and chemical properties of nanostructured (Ti-Hf-Zr-V-Nb)N coatings under different deposition conditions. Materials Chemistry and Physics. 2014;**147**(3):1079-1091. DOI: 10.1016/j.matchemphys.2014.06.062

[48] Beresnev VM, Sobol' OV, Andreev AA, Gorban' VF, Klimenko SA, Litovchenko SV, et al. Formation of

superhard state of the TiZrHfNbTaYN vacuum–arc high-entropy coating. Journal of Superhard Materials. 2018;**40**(2):102-109

[49] Liang SC, Chang ZC, Tsai DC, Lin YC, Sung HS, Deng MJ, et al. Effects of substrate temperature on the structure and mechanical properties of (TiVCrZrHf)N coatings. Applied Surface Science. 2011;**257**(17):7709-7713. DOI: 10.1016/j.apsusc.2011.04.014

[50] Huang PK, Yeh JW. Effects of substrate temperature and post-annealing on microstructure and properties of (AlCrNbSiTiV)N coatings. Thin Solid Films. 2009;**518**(1):180-184. DOI: 10.1016/j.tsf.2009.06.020

[51] Chang KS, Chen KT, Hsu CY, Da HP. Growth (AlCrNbSiTiV)N thin films on the interrupted turning and properties using DCMS and HIPIMS system. Applied Surface Science. 2018;**440**:1-7. DOI: 10.1016/j.apsusc.2018.01.110

[52] Chang CH, Li PW, Wu QQ, Wang MH, Sung CC, Hsu CY. Nanostructured and mechanical properties of high-entropy alloy nitride films prepared by magnetron sputtering at different substrate temperatures. Materials and Technologies. 2019;**34**(6):343-349

[53] Chang ZC, Liang SC, Han S. Effect of microstructure on the nanomechanical properties of TiVCrZrAl nitride films deposited by magnetron sputtering. Nuclear Instruments and Methods in Physics Research B. 2011;**269**(18):1973-1976. DOI: 10.1016/j.nimb.2011.05.027

[54] Braic M, Braic V, Balaceanu M, Zoita CN, Vladescu A, Grigore E. Characteristics of (TiAlCrNbY)C films deposited by reactive magnetron sputtering. Surface and Coatings Technology. 2010;**204**(12-13):2010-2014. DOI: 10.1016/j.surfcoat.2009.10.049

[55] Braic V, Balaceanu M, Braic M, Vladescu A, Panseri S, Russo A. Characterization of multi-principal-element (TiZrNbHfTa)N and (TiZrNbHfTa)C coatings for biomedical applications. Journal of the Mechanical Behavior of Biomedical Materials. 2012;**10**:197-205. DOI: 10.1016/j.jmbbm.2012.02.020

[56] Zhang BY, Zhou YJ, Lin JP, Chen GL, Liaw PK. Solid-solution phase formation rules for multi-component alloys. Advanced Engineering Materials. 2008;**10**(6):534-538

[57] Guo S, Ng C, Lu J, Liu CT. Effect of valence electron concentration on stability of fcc or bcc phase in high entropy alloys. Journal of Applied Physics. 2011;**109**(10)

[58] Jhong YS, Huang CW, Lin SJ. Effects of CH_4 flow ratio on the structure and properties of reactively sputtered (CrNbSiTiZr)cx coatings. Materials Chemistry and Physics. 2018;**210**:348-352. DOI: 10.1016/j.matchemphys.2017.08.002

[59] Chen TK, Wong MS. Structure and properties of reactively-sputtered AlxCoCrCuFeNi oxide films. Thin Solid Films. 2007;**516**(2-4):141-146

[60] Edlmayr V, Moser M, Walter C, Mitterer C. Thermal stability of sputtered Al_2O_3 coatings. Surface and Coatings Technology. 2010;**204**(9):1576-1581 Available from: http://www.sciencedirect.com/science/article/pii/S0257897209008019

[61] Bendavid A, Martin PJ, Jamting Å, Takikawa H. Structural and optical properties of titanium oxide thin films deposited by filtered arc deposition. Thin Solid Films. 1999;**355-356**:6-11. Available from: http://www.

sciencedirect.com/science/article/pii/S0040609099004368

[62] Fateh N, Fontalvo GA, Mitterer C. Structural and mechanical properties of dc and pulsed dc reactive magnetron sputtered V_2O_5 films. Journal of Physics D: Applied Physics. 2007;**40**(24):7716-7719

[63] Bernard O, Huntz AM, Andrieux M, Seiler W, Ji V, Poissonnet S. Synthesis, structure, microstructure and mechanical characteristics of MOCVD deposited zirconia films. Applied Surface Science. 2007;**253**(10):4626-4640. Available from: http://www.sciencedirect.com/science/article/pii/S0169433206013080

[64] Pogrebnjak AD, Beresnev VM, Smyrnova KV, Kravchenko YO, Zukowski PV, Bondarenko GG. The influence of nitrogen pressure on the fabrication of the two-phase superhard nanocomposite (TiZrNbAlYCr)N coatings. Materials Letters. 2018;**211**:316-318

[65] Tsai MH, Yeh JW, Gan JY. Diffusion barrier properties of AlMoNbSiTaTiVZr high-entropy alloy layer between copper and silicon. Thin Solid Films. 2008;**516**(16):5527-5530

[66] Huang P-K, Yeh J-W. Effects of nitrogen content on structure and mechanical properties of multi-element (AlCrNbSiTiV)N coating. Surface and Coatings Technology. 2009;**203**(13):1891-1896. DOI: 10.1016/j.surfcoat.2009.01.016

[67] Liang SC, Tsai DC, Chang ZC, Sung HS, Lin YC, Yeh YJ, et al. Structural and mechanical properties of multi-element (TiVCrZrHf)N coatings by reactive magnetron sputtering. Applied Surface Science. 2011;**258**(1):399-403. DOI: 10.1016/j.apsusc.2011.09.006

[68] Braic V, Vladescu A, Balaceanu M, Luculescu CR, Braic M. Nanostructured multi-element (TiZrNbHfTa)N and (TiZrNbHfTa)C hard coatings. Surface and Coatings Technology. 2012;**211**:117-121. DOI: 10.1016/j.surfcoat.2011.09.033

[69] Hsieh MH, Tsai MH, Shen WJ, Yeh JW. Structure and properties of two Al-Cr-Nb-Si-Ti high-entropy nitride coatings. Surface and Coatings Technology. 2013;**221**:118-123. DOI: 10.1016/j.surfcoat.2013.01.036

[70] Tsai DC, Chang ZC, Kuo BH, Shiao MH, Chang SY, Shieu FS. Structural morphology and characterization of (AlCrMoTaTi)N coating deposited via magnetron sputtering. Applied Surface Science. 2013;**282**:789-797. DOI: 10.1016/j.apsusc.2013.06.057

[71] Tsai DC, Chang ZC, Kuo BH, Chang SY, Shieu FS. Effects of silicon content on the structure and properties of (AlCrMoTaTi)N coatings by reactive magnetron sputtering. Journal of Alloys and Compounds. 2014;**616**:646-651

[72] Cheng KH, Lai CH, Lin SJ, Yeh JW. Structural and mechanical properties of multi-element (AlCrMoTaTiZr)Nxcoatings by reactive magnetron sputtering. Thin Solid Films. 2011;**519**(10):3185-3190. DOI: 10.1016/j.tsf.2010.11.034

[73] Braic V, Parau AC, Pana I, Braic M, Balaceanu M. Effects of substrate temperature and carbon content on the structure and properties of (CrCuNbTiY)C multicomponent coatings. Surface and Coatings Technology. 2014;**258**:996-1005. DOI: 10.1016/j.surfcoat.2014.07.044

[74] Shen W-J, Tsai M-H, Yeh J-W. Machining performance of sputter-deposited $(Al_{0.34}Cr_{0.22}Nb_{0.11}Si_{0.11}Ti_{0.22})$50N50 high-entropy nitride coatings. Coatings. 2015;**5**(3):312-325. Available from: http://www.mdpi.com/2079-6412/5/3/312/

[75] Bushlya V, Johansson D, Lenrick F, Ståhl J, Schultheiss F. Wear mechanisms of uncoated and coated cemented carbide tools in machining lead-free silicon brass. Wear. 2017;(376-377):143-151. DOI: 10.1016/j.wear.2017.01.039

[76] Zhang W, Tang R, Yang ZB, Liu CH, Chang H, Yang JJ, et al. Preparation, structure, and properties of high-entropy alloy multilayer coatings for nuclear fuel cladding: A case study of AlCrMoNbZr/(AlCrMoNbZr)N. Journal of Nuclear Materials. 2018;**512**:15-24. DOI: 10.1016/j.jnucmat.2018.10.001

[77] Hsueh H-T, Shen W-J, Tsai M-H, Yeh J-W. Effect of nitrogen content and substrate bias on mechanical and corrosion properties of high-entropy films (AlCrSiTiZr)100−xNx. Surface and Coatings Technology. 2012;**206**(19-20):4106-4112. Available from: http://linkinghub.elsevier.com/retrieve/pii/S0257897212002873

[78] Zhang W, Wang M, Wang L, Liu CH, Chang H, Yang JJ, et al. Interface stability, mechanical and corrosion properties of AlCrMoNbZr/(AlCrMoNbZr)N high-entropy alloy multilayer coatings under helium ion irradiation. Applied Surface Science. 2019;**485**:108-118. DOI: 10.1016/j.apsusc.2019.04.192

[79] Chang S, Chen M, Chen D. Multiprincipal-element AlCrTaTiZr-nitride nanocomposite film of extremely high thermal stability as diffusion barrier for Cu metallization. Journal of the Electrochemical Society. 2009;**156**(5):37-42